# To study the tracking efficiency performance of $J/\psi$ and $\psi'$ using CBM MuCh setup

**M.Sc. Thesis**

*By*

**Hridey Chetri**

**DISCIPLINE OF PHYSICS**

**INDIAN INSTITUTE OF TECHNOLOGY INDORE**

**JUNE 2019**

# To study the tracking efficiency performance of $J/\psi$ and $\psi'$ using CBM Much setup

**A THESIS**

*Submitted in partial fulfillment of the requirements*

*for the award of the degree*

***of***

**Master of Science**

*by*

**Hridey Chetri**

**DISCIPLINE OF PHYSICS**

**INDIAN INSTITUTE OF TECHNOLOGY INDORE**

**JUNE 2019**

Indian Institute of Technology Indore



# CANDIDATE'S DECLARATION

I hereby declare that the work presented in the thesis entitled **To study the tracking efficiency performance of $J/\psi$ and $\psi'$ using CBM Much setup** in the partial fulfillment of the requirements for the award of the Degree of **Master of Science** and submitted in the **Discipline of Physics, Indian Institute of Technology Indore** is an authentic record of my own work carried out during a period from July 2018 to June 2019 under the supervision of **Dr. Ankhi Roy**, IIT Indore. The matter presented in this thesis has not been submitted by me for the award of any other degree of this or any other Institute.

Hriday Chetri
**HRIDEY CHETRI**

This is to certify that the above statement made by the candidate is correct to the best of my/our knowledge.

Ankhi Roy
**Dr. Ankhi Roy**

................................................................................................................................

HRIDEY CHETRI has successfully given her M.Sc. Oral Examination held on 21 June, 2019.

Ankhi Roy
**Dr. Ankhi Roy**
**Date:** 28/06/2019

**Dr. Manavendra Mahato**
**Date:** 2/7/19

**Convener, DPGC**
**Date:** 2/7/19

**Dr. Preeti A. Bhobe**
**Date:** 1/7/19

# *Acknowledgements*

I would like to express my sincere gratitude to my thesis supervisor Dr. Ankhi Roy for her patience, motivation and enthusiasm for helping me to complete this thesis.

Their collaboration has given me the opportunity to work on this diverse exciting thesis and an insight to research atmosphere.

Sincere gratitude is also extended to the PSPC members Dr. Manavendro mahato and Dr. Preeti A Bhobe for their valuable remarks and kind suggestions.I would also like to acknowledge Dr. Partha Pratim Bhaduri for many fruitful discussions and useful comments.
Last but not the least, I would like to thank my lab-mates especially Sumit kr. Kundu, Sudhir Rodhe and Ravindra Singh for their constant encouragement and support and those who have helped me directly or indirectly with this thesis.

Hridey Chetri
1703151005
Discipline of Physics
Indian Institute of Technology Indore

# *Abstract*

Relativistic heavy ion collision makes it possible to study the fundamental constituents of the matter. High-resolution detectors are required to detect the rare probes like the decay of $J/\psi$ into dimuon. One such a kind is CBM detector which will be working at moderate temperature and high baryonic density of QCD phase diagram. As the detector is in a developing stage, we are trying to design the detector through simulation. In first part of the work we compared the transport engine GEANT3 and GEANT4 through point density at 12 AGeV minimum bias Au-Au collision. In second part we are trying to find the efficiency of CBM MuCh detector using the rare decay channel of dimuon through $J/\psi$. We tried finding the efficiency of $J/\psi$ in $p_T$ regime through the division of reconstructed by generated counts of dimuon. The simulation is done at 25 AGeV for $10^5$ Au-Au central collision.

# Contents

# List of Figures

# List of Tables

# Abbreviations

| | |
|---|---|
| **QCD** | **Q**uantum **C**hromodynamics |
| **QGP** | **Q**uark **G**luon **P**lasma |
| **CBM** | **C**ompressed **B**aryonic **M**atter |
| **LHC** | **L**arge **H**adron **C**ollider |
| **FAIR** | **F**acility for **A**ntiproton and **I**on **R**esearch |
| **MuCh** | **M**uon **C**hamber |

# Chapter 1

# Quark Gluon Plasma

## 1.1 Introduction

Existence of matter in nature is vivid. Various phenomena are related to the existence of matter in a different state, and they are governed by various parameters (e.g., temperature, pressure, density, etc.). The change in parameters governing the system (state of matter) may lead the system to different states. The physical and chemical properties of the matter change during the phase transition. When sufficient energy is provided to any substance, it transforms into a new ionized state with constituents of ions and free electrons known as plasma. Similarly, at the subatomic level with sufficient energy density, a new state of matter could be achieved, which is known as Quark Gluon Plasma(QGP). Quark Gluon Plasma(QGP) is a deconfined phase of quarks and gluons where quarks are free to move in localized potential. It was assumed that after the big-bang for a few second QGP state was formed [1].

As the system moves forward in time after the big bang, the hadronization process occurred. As a result of hadronization, the whole universe is created. Now, the universe is governed by four fundamental forces in nature; gravitational, electromagnetic, weak, and strong. The vector bosons which are the carrier of gravitational, electromagnetic, weak, and strong forces are graviton, photon, $W^{\pm}$, Z boson and gluon respectively. Quarks confined inside a nucleon interacts through strong interaction. According to the Standard Model of particle physics, the strong interaction is described by relativistic quantum field theory called Quantum Chromodynamics(QCD). In QCD, point-like quarks and gluons are the elementary degrees of freedom. Quarks are found in 12 flavor considering the anti-particle (up, down, strange, charm, bottom, top) and anti-quarks ( $\bar{up}$, $\bar{down}$, $\bar{strange}$, $\bar{charm}$, $\bar{bottom}$, $\bar{top}$).

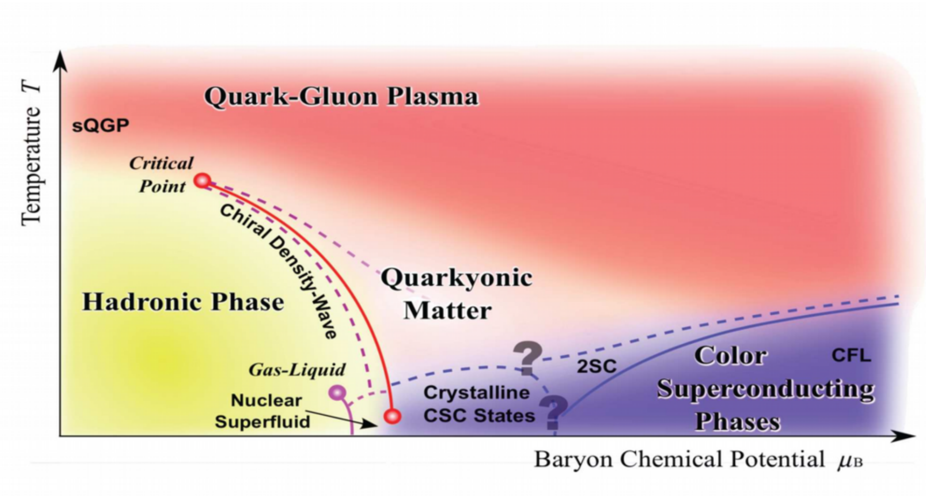


FIGURE 1.1: Schematic view of QCD phase diagram in terms of the baryon chemical potential $\mu_B$ and temperature T [1]

Quarks and gluons carry additional quantum number called color charge, due to which quarks and gluons are self-interacting. The self-interacting characteristics of quarks and gluons result in running of the QCD coupling constant $\alpha_s = \frac{g_s}{4\pi}$ with the distance between the quarks or with momentum transfer (Q), $\alpha_s$ decreases logarithmically with the increase in Q. This phenomenon is known as asymptotic freedom. Converse to the asymptotic freedom, if we increase the separation between the quarks or reduce the momentum transfer (Q), the interaction between two quarks is so strong that it creates a pair of quark and anti-quark, which results in the non-existence of single quark, which is known as infrared slavery.

Phase diagram of the strongly interacting matter as a function of the temperature T and the baryochemical potential $\mu_B$ is shown in Figure-1.1. For very low net baryon density and high temperature, where particle and anti-particles are in equal abundant the transition is expected to be a smooth crossover from hadronic to partonic matter, above a temperature of around 160 MeV [1]. It is expected that the first order phase transition occurs from hadronic to partonic matter beyond a critical endpoint, with high baryon density and moderate temperature. However, at lower temperature and very high baryonic density, as a result of high compression, a partonic phase might exist as shown in figure-1.2. Relativistic heavy ion collision experiment makes it possible to study the properties of strongly interacting matter at high baryon density or high temperature. Ultrarelativistic Heavy ion collision experiments dedicated to the exploration and characterization of a new state of subatomic matter, i.e., QGP, may include Brookhaven National Laboratory (BNL), European Organization for Nuclear Research (CERN) beginning at 1968. Recently, RHIC at (BNL), Large Hadron Collider(LHC) at (CERN) with ALICE, ATLAS, CMS, and LHCb detectors working on the different region for high temperature and very low net baryonic density.

The upcoming experimental setup at Facility for Antiproton and Ion Research (FAIR) at GSI is a fixed target experiment. The Compressed Baryonic Matter(CBM) at FAIR is designed to carry out heavy ion collisions with $\sqrt{s}$ close to 10 AGeV. One of the experimental setups CBM at FAIR is also going to study the QCD phase diagram at around moderate temperature and high baryonic density [1]. The research program devoted to the exploration of compressed baryonic matter will start with primary beams from the SIS100 synchrotron (protons up to 29 GeV, Au up to 11 AGeV, nuclei with Z/A = 0.5 up to 14 AGeV), and will be continued with beams from the SIS300 synchrotron (protons up to 90 GeV, Au up to 35 AGeV, nuclei with Z/A = 0.5 up to 45 AGeV). The layout of FAIR is presented in Fig. 2.1. The beam extracted to the CBM cave reaches intensities up to $10^9$ Au ions per second [2].

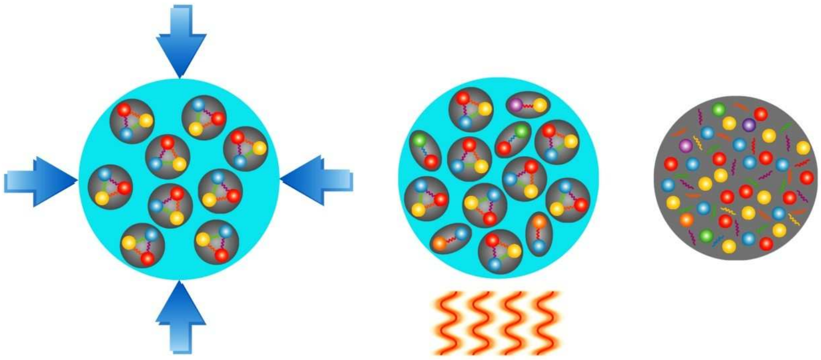

FIGURE 1.2: Schematic view of the QGP formation due to extreme compression and excessive heating [4].

## 1.2 Relativistic Heavy Ion Collisions

Relativistic heavy ion collision experiments provide the opportunity to study the properties of strongly interacting matter at high energy. In the laboratory, by colliding heavy ions at relativistic velocity at various energies, one can produce nuclear matter over a range of temperatures and densities [5].

### 1.2.1 Space-time picture of relativistic heavy ion collisions

As shown in the figure-1.3, the collision process can be explained in following steps from an initial state, pre-equilibrium, thermalization, hadronization, and freeze out. Initially, two Lorentz-contracted nuclei at relativistic velocity travel along the light cone, and they collide with each other, due to the inelastic collision, a large amount of energy is deposited inside a small volume. A large number of partons (quarks and gluons) are liberated from the high energy deposition. In the preequilibrium state, these partons interact among themselves with a characteristic mean free path much smaller compared to the size of the system. After sufficient reinteractions for $\tau_o$ ~0.5-1fm/c, the quarks and gluons undergo equilibration, and one can expect

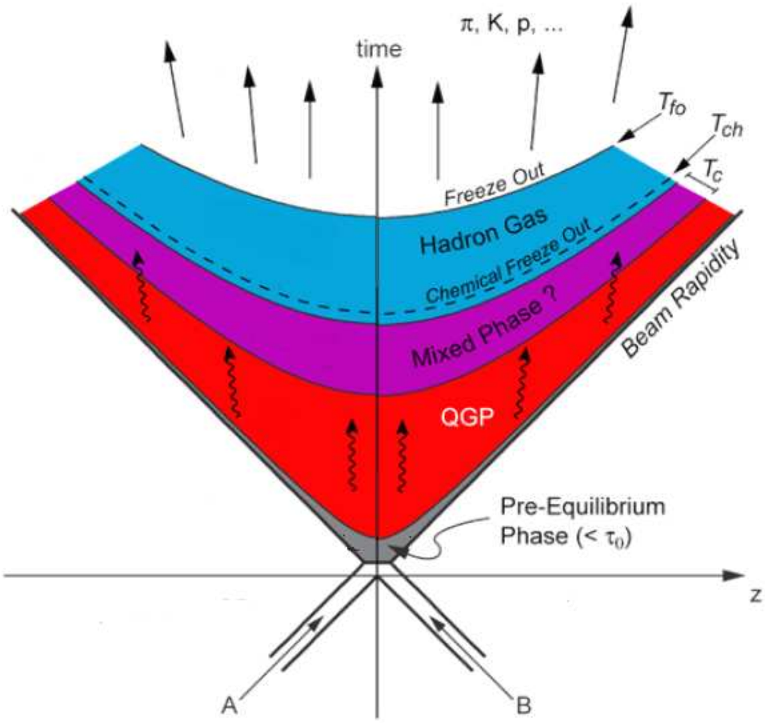


FIGURE 1.3: A schematic diagram showing the evolution of the fireball produced in relativistic heavy ion collisions in the light cone picture [1].

the formation of Quark-Gluon Plasma (QGP). Due to the pressure gradient the QGP expands and cools (for a duration of $\tau_{QGP} \sim$ 3-5fm/c). As energy density falls below the critical value ( $\epsilon_c \sim$1 GeV/$fm^3$ ) hadronization starts at a certain point "chemical freezeout" occurs at which inelastic interaction ceases, and no more hadrons are formed. At later stage kinetic freeze-out occurs, it is the point where the mean free path $\lambda = \frac{1}{n\sigma}$ of the particles is larger than the system size, or in other words, elastic interaction ceases. After kinetic freezeout particles move towards the detector to be detected. Due to the short lifetime of the medium, special probes are needed to access the properties of the medium [5].

## 1.3 Signatures of QGP in Relativistic Nuclear Collisions

Since QGP is a plasma state with a very short lifetime, direct detection of QGP is not possible. So one has to look for the signals to search for the evidence for the QGP formation via indirect means. Some of the experimental signals which have been proposed over the years to probe the matter created in heavy ion collisions are.

### 1.3.1 Quarkonium suppression

Quarkonia is the bound state of quark and antiquark, suppression in the counts of quarkonium(like J/$\psi$ and $\Upsilon$) also serve as the signature of the formation of QGP. Charmonium or bottonium are produced at the early stage of the collision in the hard scattering process. As q$\bar{q}$ moves through QGP their bound state is loosening or broken up due to the presence of other colored quarks, and anti-quarks in the produced medium. This effect is known as the Debye screening effect. One can use the behavior of $J/\psi$ to probe if a quark-gluon plasma was formed in the collision. As $J/\psi$ have small radii as compared to other hadrons, they are supposed to survive beyond the QGP phase transition up to some higher temperature, at which they will become dissociated. With the help of the dissociation temperature of $J/\psi$, one can estimate the temperature and energy of QGP medium [6]. To find the dissociation temperature of $J/\psi$, we can approach in two ways. One Schwinger model and the other is the lattice potential model. In the former approach $q\bar{q}$ is considered as non-relativistic system due to their heavy mass($m_Q >> \Lambda_{QCD} \sim 200 MeV$). One can solve the Schrodinger equation taking time-dependent potential.

$$-\frac{1}{m}\bigtriangledown^2\Psi_i(r) + V(r)\Psi_i(r) = (M_i - 2m)\Psi_i(r) \tag{1.1}$$

V(r, T)= $\sigma$r $\frac{1-e^{-\mu r}}{\mu r}$ - $\frac{\alpha}{r}$ $e^{-\mu r}$ $\quad\quad$ $\mu = \frac{1}{r_D(T)}$ is the screening mass.

The other methods start from partition function Z, which is related to the free energy by Z = exp($-\beta$F ); this in turn gives the thermodynamic potentials

$$F = U - TS; \quad S = -(\frac{\partial F}{\partial T})_V; \quad U(r,T) = F(r,T) - T(\frac{\partial F(r,T)}{\partial T})_V \tag{1.2}$$

Considering internal energy U (r, T ) provides the temperature dependence potential. The results obtained by Schwinger model states that excited state $\psi'$ and $\chi_c$ dissociate at around $T \simeq T_c$ and $J/\psi$ at around $T \simeq 1.2T_c$. The result given by lattice potential model says that $\psi'$ and $\chi_c$ dissociate at around $T \simeq 1.1T_c$ and $J/\psi$ at around $T \simeq 2T_c$. The results from both the model well matches for the excited states whereas for $J/\psi$ Lattice potential model shows higher dissociation temperature. The reason for this is that the internal energy U (r, T ) leads to much stronger binding than the Schwinger model potential [4].

### 1.3.2 Global Observables

Global observables like transverse energy $E_T$, particle multiplicities (N, $N_{ch}$ etc.), $p_T$ spectra of the produced particles and their pseudo-rapidity distributions with the mass number and beam energy provide insight about the dynamics of the system and regarding the formation of QGP. It is found that according to Landau's hydrodynamic model except at the phase transition points, the rapidity density linearly scales with $< p_T >$. The temperature remains constant at point of transition whereas $p_T$ will show a plateau with an increase of entropy indicating of QGP phase and the order of phase transition [1].

### 1.3.3 Strangeness enhancement

In the QGP, the quarks and anti-quarks, and the gluons, continuously react with each other via the following processes:

$$gg- > q\bar{q}, q\bar{q}- > gg, q\bar{q}- > q^{'}\bar{q^{'}} \tag{1.3}$$

Through this interaction, it is supposed that chiral symmetry is restored due to the formation of QGP, then s and $\bar{s}$ should have nearly the same abundance as u, $\bar{u}$ and d, $\bar{d}$ in the plasma, because the masses of u, d and s quarks are nearly equal. Therefore, in the heavy-ion collision, strangeness should be enhanced [6].

### 1.3.4 Electromagnetic radiations: Photons and Dilepton

Dileptons produced during the process serves as the reliable probes, as they interact electromagnetically with the produced medium. Therefore, their interaction cross-section is small in comparison to hadrons and has larger mean-free path than the QGP system. So, they come out unmodified from the dense fire-ball carrying the information about the initial state of the system. Similar to dileptons, photons also interact electromagnetically with the rest of the system. Therefore, the mean free path of the photon is quite large, and hence, the photon might not lose much energy-momentum after it is produced. So photon also serves as reliable probes [7].

### 1.3.5 Jet Quenching

The characteristic collimated spray of hadrons resulting from the fragmentation of an outgoing parton is called a 'jet'. While propagating through the fireball, they lose their energy through interaction with the fireball, which results in the attenuation of collimated spray. Which is known as "jet Quenching" [7].

### 1.3.6 Elliptic Flow

Elliptic flow results from the pressure gradient created by non-central collision in the QGP medium. It is defined as the second coefficient of Fourier expansion, and it is given by

$$v_2 =< cos[2(\phi - \Psi)] >=< \frac{p_x^2 - p_y^2}{p_t^2} > \tag{1.4}$$

It is studied to look for the thermalization of the produced medium [2].

### 1.3.7 Organization and motivation of the thesis

The focal aim of the relativistic heavy ion collision experiments is to explore the QCD phase diagram and to identify the formation of quark-gluon plasma in the laboratory. The CBM experiment at FAIR is designed to unravel the phase structure of nuclear matter in the region of moderate temperatures and extremely high net baryon densities. Since the CBM experiment is in the developing stage, one can contribute towards the development of the experimental detectors through analyzing and simulating more realistically by running the CBM chain using different geometry setup and transport engine. This work is divided into two parts.
i) We are trying to compare between the different transport model(i.e., GEANT3 and GEANT4)
ii)Tracking Efficiency of MuCh detector of CBM in different kinematics region using the dimuon channel. In this thesis 2nd chapter is dedicated to Experimental setup of CBM, 3rd for Simulation procedure of MuCh, 4th for Analysis and concluding with 5th chapter with Results and future outlooks. The motivation behind this work is that we are trying to contribute towards the devlopment of MuCh detector in CBM experiment. In doing so we are running MuCh simulation chain with different setup of geometries and different transport engines model.

# Chapter 2

# The Compressed Baryonic Matter Experiment

## 2.1 Introduction

Relativistic heavy ion collision experiments give us the opportunity to produce and study a new state of matter known as QGP in the laboratory. The upcoming Compressed Baryonic Matter (CBM) experiment, at the future accelerator Facility for Antiproton and Ion Research (FAIR) at GSI, Darmstadt aims at the production and characterization of such kind of matter at moderate temperatures and extremely high baryonic densities. CBM is one of the major experimental setups at FAIR among the other experiments like PANDA, NUSTAR, and HESR, as shown in figure-2.1. The challenge of CBM experiment at the FAIR is the measurement of rare particles in among the high multiplicity particles and the observables governing the particle dynamics, using the high-intensity heavy ion beams provided by the accelerators SIS-100 and SIS-300 at FAIR [1].

The CBM experiment at FAIR is solely dedicated to studying the QGP state formed by high compression of nuclear matter. According to transport code calculation, it

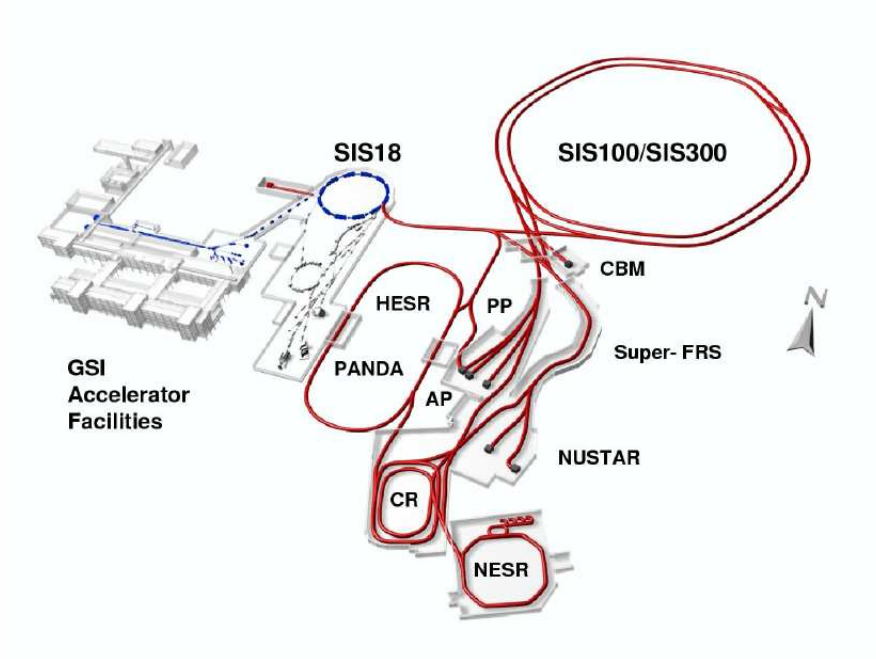


FIGURE 2.1: Layout of the Facility for Antiproton and Ion Research (FAIR) [1].

is seen that seven times the saturation density can be achieved. In this process of phase transition from hadronic to partonic state, the nucleons are compressed in a small volume, due to which a mixed phase of baryons and partons occurs, before it goes to QGP state [3].

## 2.2 The Compressed Baryonic Matter (CBM) experimental setup

The CBM experiment is designed to measure the multiplicities, phase-space distributions, and flow of protons, pions, charmonium, and other vector bosons. The main objective of the CBM experiment is to extract out rare probes at reaction rate 10 MHz with multiplicities of the particle to be around 1000 per event. The unique features of CBM detector system are self-triggered read-out electronics, a high-speed data processing, and acquisition system, fast algorithms, and radiation hard detectors [1]. The various detector used in CBM experimental setup as shown in figure-2.3 are discussed in the following subsection:

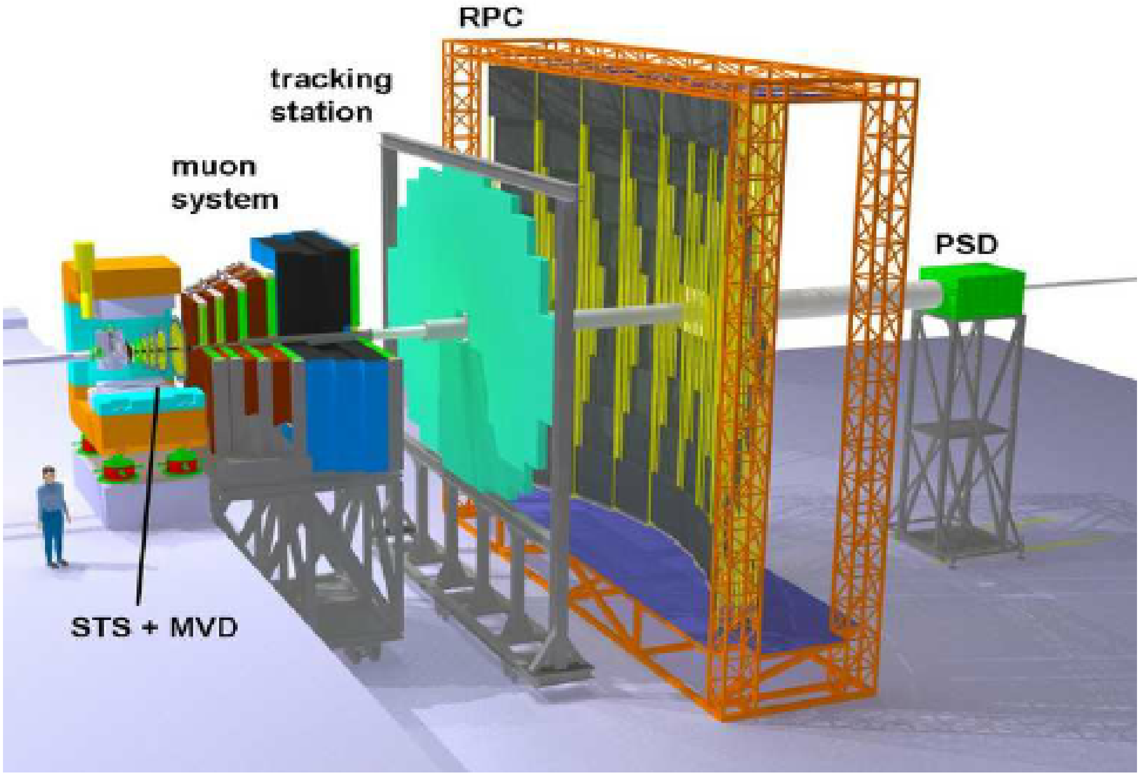


FIGURE 2.2: Layout of CBM experimental setup [3].

### 2.2.1 Dipole magnet

The Dipole magnet used here can produce the bending power of 1 - 2 Tm. It has a large aperture (acceptance) of $\pm 25^o$ polar angle, and the field region is confined within 1 m along the beam axis. The coil shape consists of two half-circles (radius= 0.5 cm) connected by a 12 cm long straight section. To produce the required field around $\sim$ 3000 A of current will be supplied to the coil and to minimize the operation cost superconductors will be used [1].

### 2.2.2 Micro-Vertex Detector (MVD)

Monolithic Active Pixel Sensors (MAPS) meets the requirements of the detector demand for excellent position resolution and a very low material budget to reduce multiple scattering. A vacuum compatible MAPS detector stations are constructed which will be around 300 - 500 $\mu$m thick silicon equivalent for sensors. The MVD consists of 3 MAPS layers located at 5, 10, and 15 cm downstream of the target. Secondary decay vertex of mesons is determined with high resolution [3].

### 2.2.3 Silicon Tracking System (STS)

It is designed for track reconstruction, determination of the event multiplicity, measurement of the momentum of charged particles from the track curvature. The detector is to be built with a low material budget and good precision of track fit. The required momentum resolution is of the order of $\Delta$p/p = 1%. They are located in between 30 to 100 cm downstream of the target inside the magnetic field [3].

### 2.2.4 Ring Imaging Cherenkov Detector (RICH)

The RICH detector mainly consists of 2.9-meter long gas vessel filled with nitrogen as a radiator material, a glass mirror, and two photodetector planes. It mainly identifies the electrons and tries to suppress pions in the momentum range below 10 GeV/c. A gaseous RICH detector is used in a standard projective geometry with focusing mirror elements and a photo detector [3].

### 2.2.5 Muon Chamber System (MUCH)

MuCh is designed to identify muon pairs in a wide range of beam energies from low energies at SIS-100 to SIS-300. Unlike other HEP detectors, in Much detector absorber are sliced, and detector stations are sandwich between the absorber as shown in figure-2.4. Number of stations and absorbers are increased according to the increment in energy. In MuCh configuration, the first absorber is 60 cm thick made of carbon and subsequent absorber of iron of thickness (20 + 20 + 30 + 35 + 100) cm according to the need of synchrotron. Each tracking station consists of three Gas Electron Multiplier(GEM) foil, the idea of GEM is based on the multiplication of electron due to ionization of the gas. The active area covered by each detector layer has been divided into trapezoidal sector-shaped modules which are supported by the external structure of 2mm thickness, as shown in figure-2.5.

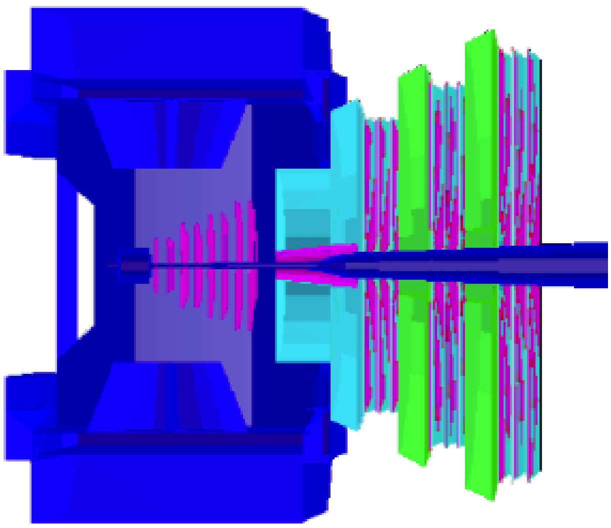

FIGURE 2.3: A schematic view of MUCH SIS100-A layout. It consists of 9 detector layers and 3 absorbers including the first absorber of 60 cm carbon [3].

Gasious medium is used in each layer of chamber as an active component to create avalanche due to ionisation when particle passes through the gas. The distance between the chamber centers is 10 cm to provide enough space for accommodating the detector profile that includes electronics boards, mechanics, a cooling arrangement, among others [14].

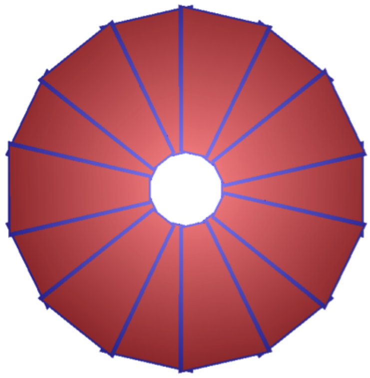

FIGURE 2.4: Schematic view of the layout of the muon chambers with trapezoidal overlapping sectors.

### 2.2.6 Transition Radiation Detector (TRD)

TRD identifies the electrons and positrons with p > 1.5 GeV/c. The detector is developed to make it more efficient for the identification of electrons. TRD readouts the particles using rectangular pads with a resolution of 300-500 $\mu m$ across the pads. The electron efficiency is found to be around 90% with 12 TRD layers.

### 2.2.7 Timing Multi-gap Resistive Plate Chambers (MRPC)

It is designed to identify hadrons using an array of Resistive Plate Chambers, which will measure the time of flight (TOF). The TOF wall covers an active area of about 120 $m^2$ and is located about 6 m downstream of the target for measurements at SIS100, and 10 m at SIS300. The required time resolution is on the order of 80 ps [1].

### 2.2.8 Electromagnetic Calorimeter (ECAL)

A shashlik type of calorimeter is used to measure photons and neutral mesons ($\pi^o$, $\eta$) decaying into photons. The ECAL will be composed of modules which consist of

140 layers of 1mm lead and 1mm scintillator, with cell sizes of $3 \times 3\ cm^2$ , $6 \times 6\ cm^2$ , and $12 \times 12\ cm^2$ [3].

### 2.2.9 Projectile Spectator Detector (PSD)

The collision centrality and orientation of the reaction plane are determined using PSD. A well- Defined reaction plane is required to study the collective flow which has to be determined by non-interacting nucleons from a projectile nucleus in nucleus-nucleus collisions. The calorimeter comprises 44 individual modules, each consisting of 60 lead/scintillator layers with a surface of $20 \times 20 cm^2$ [3].

### 2.2.10 Online event selection and data acquisition

As the detector interaction is 10 MHz, a high-speed data acquisition computer system is required to measure the high data rate from the detector. The event selection system will be based on a fast online event reconstruction running on a PC farm equipped with many-core CPUs and graphics cards. Track reconstruction is done by parallel track finding and fitting algorithms, implementing the Cellular Automation and Kalman Filter [3].

# Chapter 3

# Simulation procedure of MUCH

One can run the CBM MuCh chain using UrQMD [12] event generator for input and default transport engine GEANT3. The process consist of following steps:(a) geometry implementation and transport (b) segmentation and digitization (c) hit formation (d) track propagation in MUCH chambers and (e) selection of tracks as muon candidates (f) di-muon analysis(for muons) as shown in the figure-3.1.

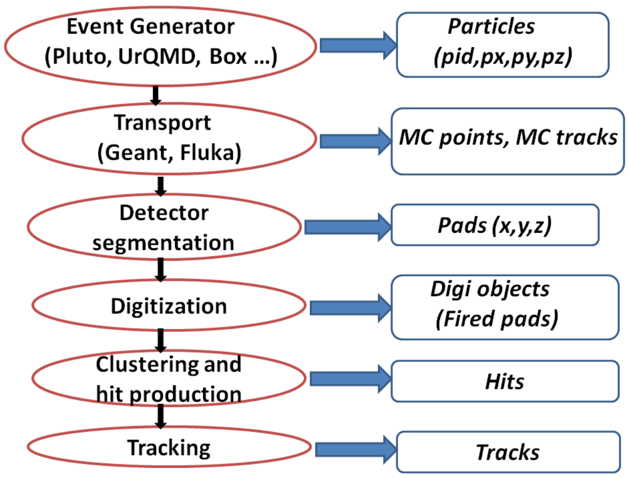


FIGURE 3.1: Schematic layout of the simulation chain in MUCH [14].

## 3.1 Segmentation,digitization, clustering and hit formation

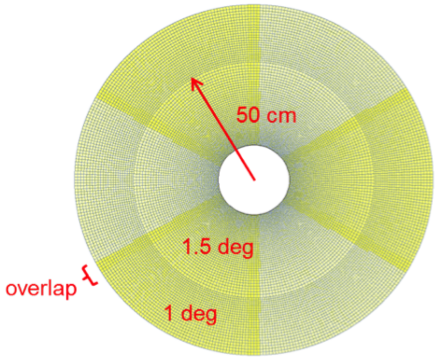


FIGURE 3.2: Schematic views of the segmentations of a layer [14].

Segmentation study is done to get the layout of the detector in a more realistic and optimized manner. The detector of MuCh is segmented in different annular planes and divided into pads of the suitable size to get desired pad occupancy to deal against the hit density($\propto \frac{1}{r}$) along the radius from beam pipe. As shown in the figure-3.2 The annular plane can be divided into pads of uniform or varying angular regions. The angular separation on the annular plane determines the pad dimension. The response of Gas Electron Multiplier(GEM) detector is known as digitization, which is based on ionization and avalanche created by particles passing through the gas. Digitization determines the Primary electron for each Monte-Carlo point and secondary electron emitted in an avalanche. It also determines the charge arrived at the pad and the spot of intersection by the secondary electron. The charge information collected at the pad is converted into ADC channels with: Amplitude with the flash discriminator, Wilkinson integration, or time-over-threshold approach. The digits form by digitization are clubbed together to form cluster and cluster are transform into hits with a suitable algorithm. [14].

## 3.2 MUCH Track Reconstruction

A high density of charged particles is the challenge for CBM-MuCh detector, which leads to high track and hit density(figure-3.3). The algorithm in MuCh is based on track reconstruction using STS as seeds. Cellular automation method is used for track reconstruction and Kalman filter technique and is used for the estimation of track parameters and trajectory recognition [14].

### 3.2.1 Track Propagation

This algorithm is used to estimate the trajectory of particles taking into account energy loss, multiple scattering, and the influence of the magnetic field. Ionization and bremsstrahlung method is used to estimate energy loss. The Equation of motion defines the propagation trajectory. The equation of motion is solved applying the $4^{th}$ order Runge-Kutta method if the track passes through the magnetic field.

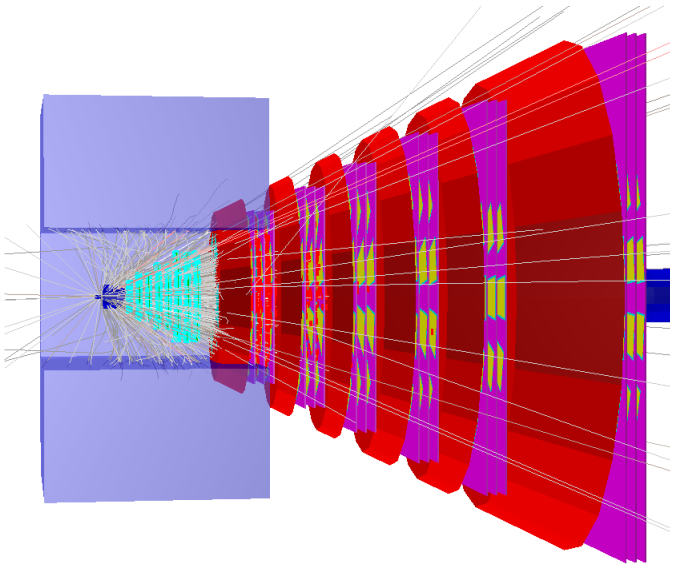

FIGURE 3.3: Visualization of simulated central collision. [14]

### 3.2.2 Track finding and fitting

The algorithm used in finding the tracks, hits are attached to the propagated track at each station. The two methods used for track finding are; one is to consider the nearest hit to the track, and the other taking all the hits within a particular environment. Kalman filter is used to construct track by connecting the hits from each station. [3].

### 3.2.3 MuCh Reconstruction Performance

The algorithm in selecting the track from similar sets of hits and random sets of hits is divided two methods; first tracks are sorted by their quality which is defined by the track length and $\chi^2$ distribution. Then the quality track is considered, and other tracks are rejected. If the number of hits shared with other tracks is more than 15%, then tracks are rejected. The track reconstruction efficiency is given by Efficiency=$N_{recons}/N_{accep}$ . $N_{recons}$ and $N_{accep}$ are the number of correctly found tracks after reconstruction and number of reconstructable tracks.

## 3.3 Muon identification and analysis

The reduction of background is made by applying appropriate cuts at the analysis level to select the muons. The cuts are; the number of hits in STS and $\chi^2$ of the STS segment, number of much layers, $\chi^2$ of MUCH segment and $\chi^2_{vertex}$.

### 3.3.1 Optimization of cuts

One should optimize the cuts to reduce background and to select the required signal in this case muon. The above mention cuts should be optimized to a certain value.

Experiments have found that 6 STS hits and $\chi^2$ less than 2.0 show a significant reduction in the background and less affecting the signal [3].

# Chapter 4

# Analysis

In this chapter of analysis, we are going compare between two different transport engine and obtain their effect in particle production. Also, we are going find out the efficiency of MuCh detector via dimuon channel.

## 4.1 Comparison of GEANT3 and GEANT4

In this part of the simulation, we are going to compare between GEANT3 and GEANT4 model of transport engine. For this purpose, we are comparing the point density per event through Monte Carlo data of each station using two transport engine. And comparison of momentum ($p$) and transverse momentum ($p_T$) distribution against counts/event for each station is done.

For our present analysis, we have employed SIS-100B(Realistic Version (v18a) with PCB cooling plates) which comprises of 4 GEM stations each containing three layers. We take $10^5$ UrQMD [12] events of minimum-bias Au-Au collision for 12 AGeV energy.

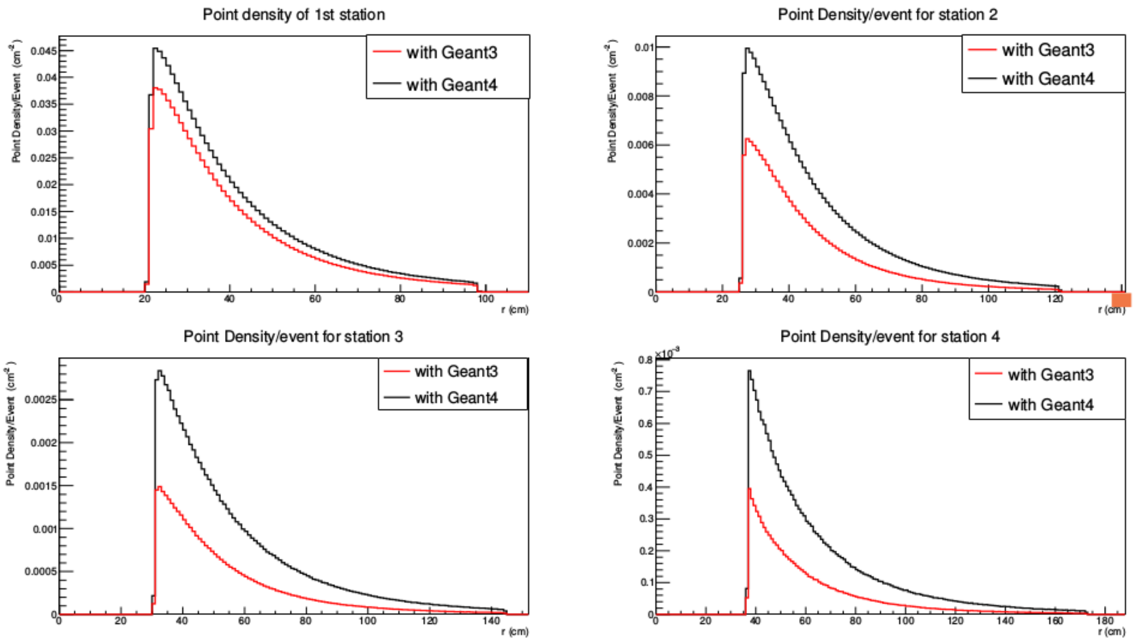


FIGURE 4.1: Point density per event of station; 1st(top left), 2nd(top right), 3rd(bottom left) and 4th(bottom right)

TABLE 4.1: Point density per event at each station for primary and secondary particles

| GEANT3 GEANT4 | St1 | St2 | St3 | St4 |
|---|---|---|---|---|
| No. of Particles/event | 225.23 | 43.62 | 12.85 | 3.44 |
| | 276.90 | 77.67 | 28.45 | 8.36 |
| No. of Primary particles/event | 11.19 | 2.88 | 0.79 | 0.13 |
| | 10.96 | 2.70 | 0.66 | 0.08 |
| No. of Secondary particles/event | 214.03 | 40.74 | 12.06 | 3.31 |
| | 265.94 | 74.96 | 27.7 | 8.27 |

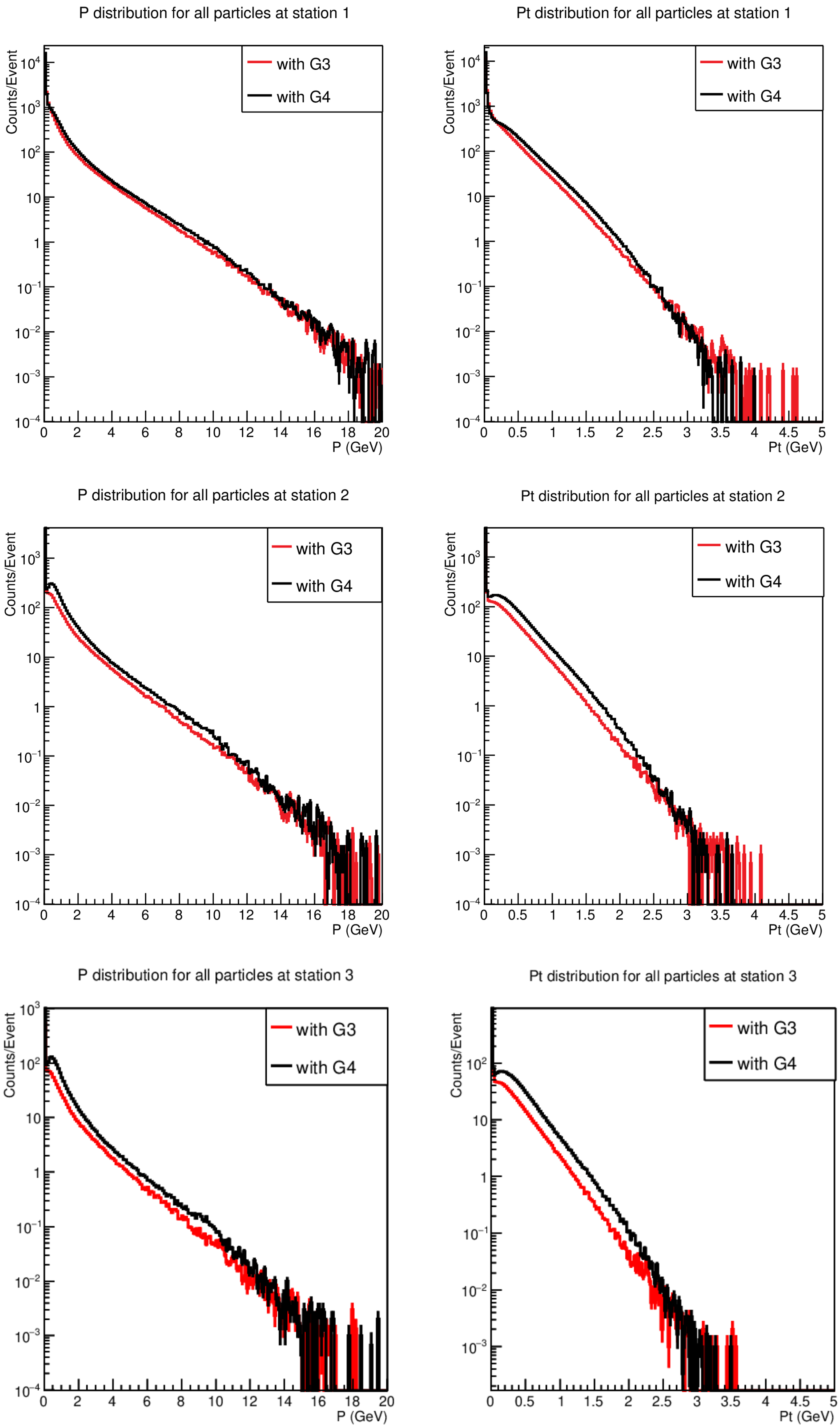




FIGURE 4.2: p and pt distribution of 1st, 2nd and 3rd station

From the plot in figure-4.1 and table no.-4.1, we can see that the point density per event of secondary particles is increased in the use of GEANT4 instead of GEANT3. But considering the point density per event of primary particles remain the same. It is also seen from $p$, and $p_T$ distribution(figure-4.2) counts per event from the use of GEANT4 is slightly higher than GEANT3.

### 4.1.1 Signal to background ratio of $J/\psi$

Here, we are trying to find signal to baground ratio for $J/\psi$. It is done so to check the value of cuts or hits to be applied in STS and MuCh to get the optimized reduction in background. First we plot the different invariant mass spectra of $J/\psi$ with different values of cuts or hits in STS, MuCh and $\chi^2$ distributions. In our study, the event generators PLUTO [16] and UrQMD [12] have been used for generating signals and background respectively. The geometry used is v18a setup and GEANT3 transport engine. We have taken 20000 events of Au-Au central collision at 25 AGeV. In the present analysis tracks are selected as :

TABLE 4.2: Tracks and cuts applied for invariant mass spectra

| Sl No. | cuts/tracks | Values |
|---|---|---|
| 1. | STS Hits | $> 6$ |
| 2. | Muon Hits | $> 11$ |
| 3. | $\chi^2_{STS}$ | $<= 1.5$ |
| 4. | $\chi^2_{MUCH}$ | $<= 1.5$ |
| 5. | $\chi^2_{VERTEX}$ | $<= 2$ |

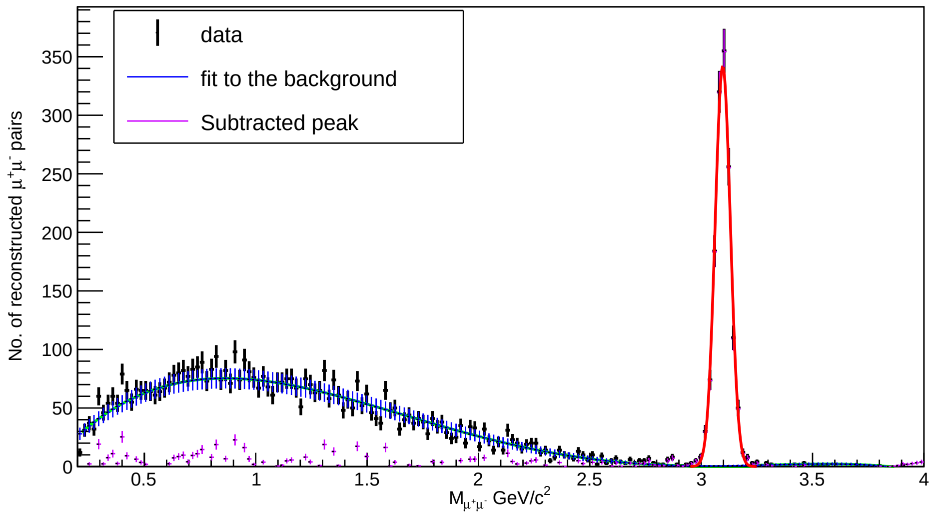


FIGURE 4.3: Fitting of signal+background of $J/\psi$

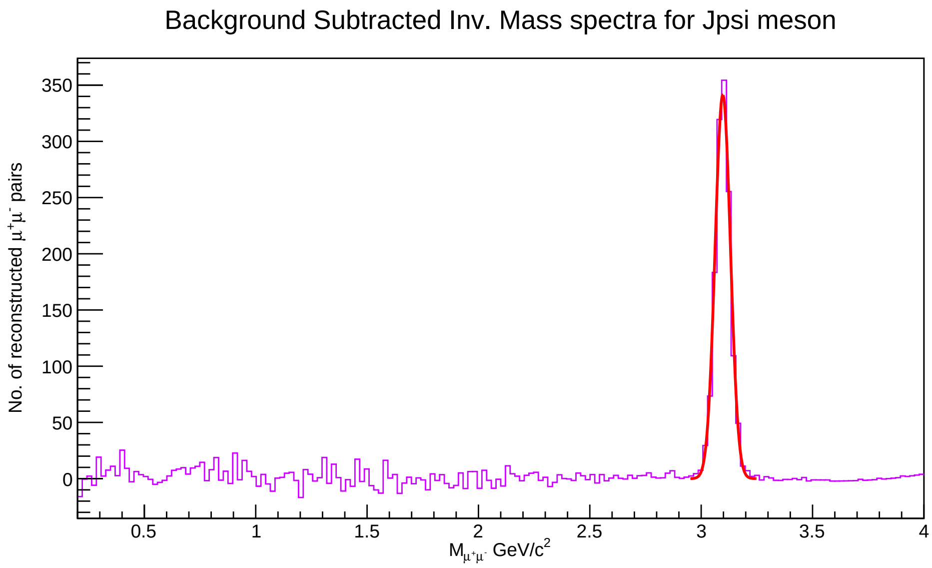


FIGURE 4.4: Background Subtracted Inv. Mass spectra for Jpsi meson

The background is fitted with polynomial function and the signal with Gaussian function in the region of $\mu \pm 3\sigma$ in figure-4.3. It is found the signal to background ratio to be around $\sim 16.67$ with applied cuts and tracks in table no-4.2. From the fitting figure-4.3, we have subtracted the background and tried extracting the signal only as shown in figure-4.4.

## 4.2 Efficiency of $J/\psi$ and $\psi'$

### 4.2.1 $p_T$ dependence of Acceptance and tracking the efficiency of J/$\psi$ and $\psi'$

In this analysis, first, the counts of $J/\psi$ and $\psi'$ for generated as well as reconstructed are divided in ten equal $p_T$ bins from 0.00 to 3.50 GeV/c(figure-4.5). To obtain efficiency, the counts of reconstructed $J/\psi$ and $\psi'$ is divided by generated counts of $J/\psi$ and $\psi'$. The plot of efficiency is shown in figure-4.6. Considering efficiency the corrected yield is calculated, which is tabulated in table no-4.3 for each bins using the formula. Corrected yield=(raw yield * branching ratio)/efficiency. The raw yield and corrected yield per event is shown in figure-4.7. For this simulation, we have taken $10^5$ events of Au-Au central collision at 25 AGeV energy. UrQMD [12] and Pluto [16] event generator are used for input background and signal, respectively. The geometry setup used is v18a and transport engine is GEANT3.

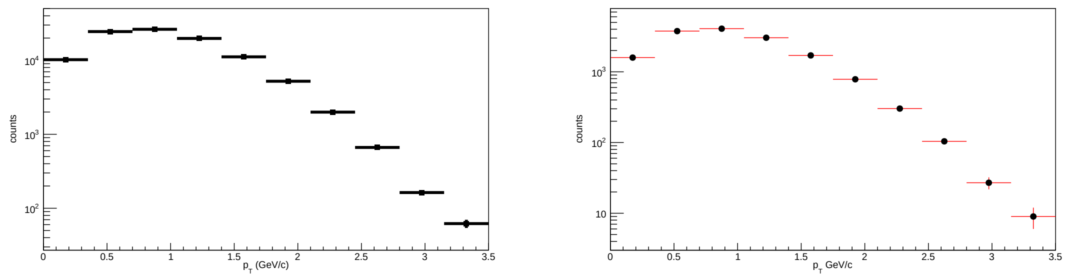

(a) Generated $p_T$ spectra

(b) Reconstructed $p_T$ spectra

FIGURE 4.5: $p_T$ spectra for $J/\psi$

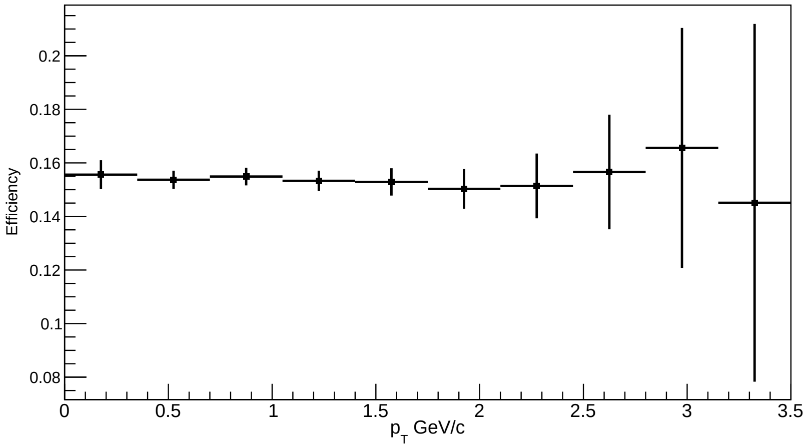


FIGURE 4.6: Efficiency plot of $J/\psi$

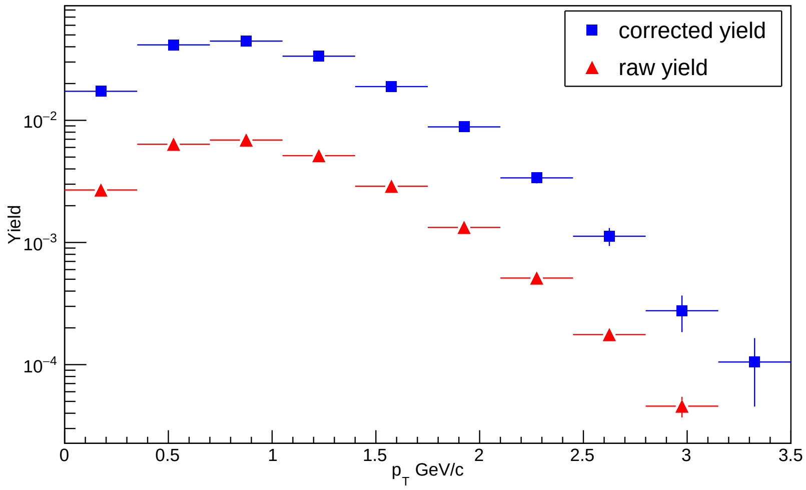


FIGURE 4.7: Raw and corrected yield of $J/\psi$

| SN | Gen | Gen Err | RC | RC Err | Eff | Eff Err | Y($10^{-5}$) | Y Err |
|---|---|---|---|---|---|---|---|---|
| 1. | 10205 | 101.01 | 1588 | 39.84 | 0.1556 | 0.0054 | 1729.13 | 15.14 |
| 2. | 24474 | 156.44 | 3762 | 61.33 | 0.1537 | 0.0034 | 4146.97 | 23.56 |
| 3. | 26282 | 162.11 | 4072 | 63.81 | 0.1549 | 0.0033 | 4453.93 | 24.32 |
| 4. | 19776 | 140.62 | 3032 | 55.06 | 0.1533 | 0.0038 | 3350.99 | 21.21 |
| 5. | 11148 | 105.58 | 1705 | 41.29 | 0.1529 | 0.0051 | 1889.31 | 15.96 |
| 6. | 5215 | 72.21 | 784 | 28.00 | 0.1503 | 0.0074 | 883.77 | 11.03 |
| 7. | 1994 | 44.65 | 302 | 17.37 | 0.1514 | 0.0121 | 337.96 | 6.84 |
| 8. | 664 | 25.76 | 104 | 10.19 | 0.1566 | 0.0214 | 112.51 | 3.97 |
| 9. | 163 | 12.76 | 27 | 5.19 | 0.1656 | 0.0448 | 27.62 | 2.11 |
| 10. | 62 | 7.87 | 9 | 3 | 0.1451 | 0.0668 | 10.50 | 1.67 |

Note: Gen=Generated, RC=Reconstructed, Eff=Efficiency, Err=Error, Y=Yield/event

Similar simulation is done for $\psi'$ as in $J/\psi$ and division of $p_T$ spectra is shown in figure-4.8. Figure-4.9 and figure-4.10 also shows the efficiency and yield of $\psi'$

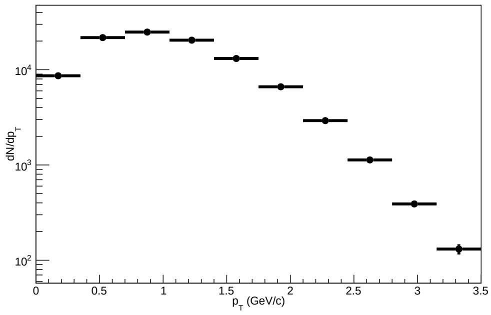


(a) Generated $p_T$ spectra

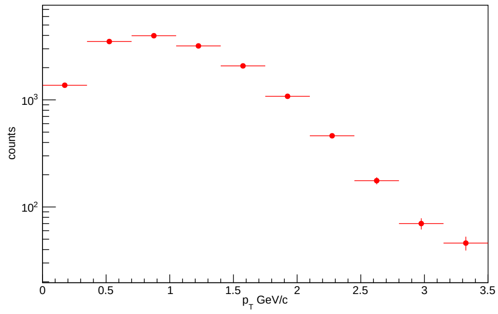


(b) Reconstructed $p_T$ spectra

FIGURE 4.8: $p_T$ spectra for $\psi'$

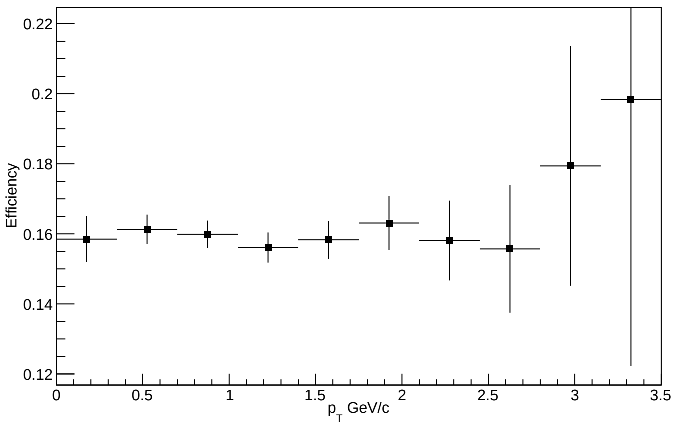


FIGURE 4.9: Efficiency plot of $\psi'$

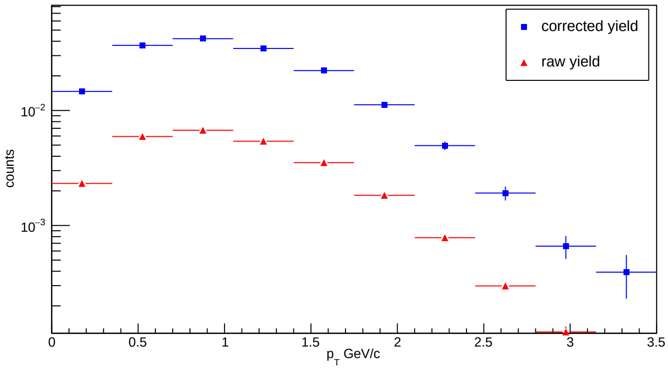


FIGURE 4.10: Raw and corrected yield of $\psi'$

| SN | Gen. | Gen Err | RC | RC Err | Eff. | Eff Err | Y($10^{-5}$) | Y Err |
|---|---|---|---|---|---|---|---|---|
| 1. | 8640 | 131.45 | 1370 | 37.01 | 0.1585 | 0.0066 | 1464.46 | 4.60 |
| 2. | 21733 | 208.48 | 3507 | 59.21 | 0.1613 | 0.0042 | 3683.73 | 7.25 |
| 3. | 24848 | 222.92 | 3974 | 63.03 | 0.1599 | 0.0043 | 4210.81 | 7.78 |
| 4. | 20433 | 202.14 | 3191 | 56.48 | 0.1561 | 0.0038 | 3463.46 | 7.12 |
| 5. | 13115 | 161.95 | 2077 | 45.57 | 0.1583 | 0.0054 | 2223.01 | 5.67 |
| 6. | 6621 | 57.4 | 1080 | 32.86 | 0.1631 | 0.0077 | 1121.90 | 3.98 |
| 7. | 2921 | 76.43 | 462 | 21.49 | 0.1581 | 0.0114 | 495.10 | 2.68 |
| 8. | 1130 | 23.81 | 176 | 13.26 | 0.1557 | 0.0182 | 191.51 | 1.67 |
| 9. | 390 | 27.92 | 70 | 8.36 | 0.1794 | 0.0342 | 66.10 | 0.93 |
| 10. | 131 | 16.17 | 26 | 6.78 | 0.1984 | 0.0762 | 39.28 | 0.65 |

TABLE 4.4: Calculated values of yield for $\psi'$

Note: Gen=Generated, RC=Reconstructed, Eff=Efficiency, Err=Error, Y=Yield/event

We have plotted the Efficiency plot from generated and reconstructed $p_T$ spectra for both $J/\psi$ and $\psi'$. From raw yield and efficiency, we found the corrected yield, and the values are tabulated in table no. 4.3 and 4.4. Here we found the efficiency in $p_T$ regime to be around 15% for both $J/\psi$ and $\psi'$.

### 4.2.2 Rapidity(y) dependence of Acceptance and tracking efficiency of J/$\psi$ and $\psi'$

Similar to analysis of $p_T$ spectra for both the particles, the setups and datas are same. However, here the mid rapidity is $\sim$ 2.01, so we have divided reconstructed and generated rapidity spectra into ten equal bins from 1.10 to 2.90(figure-4.11 and 4.14 ). We divided counts of reconstructed of $J/\psi$ and $\psi'$ by generated to get efficiency(figure-4.12 and 4.15). After that using the formula for yield we calculated the yield as shown in figure-4.13 and figure-4.16 respectively.

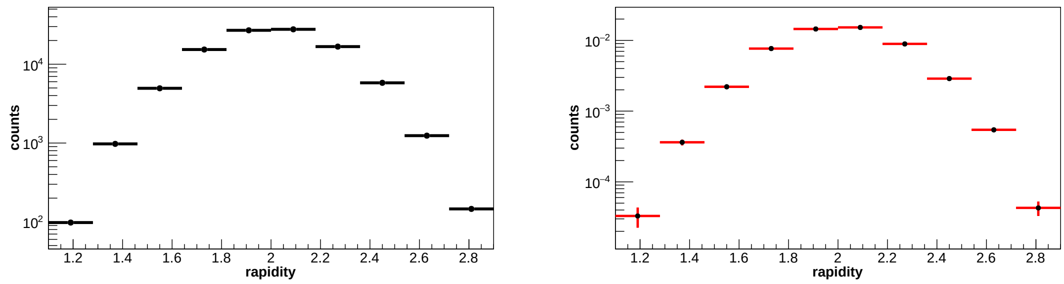


(a) Generated rapidity spectra

(b) Reconstructed rapidity spectra

FIGURE 4.11: Rapidity spectra for $J/\psi$

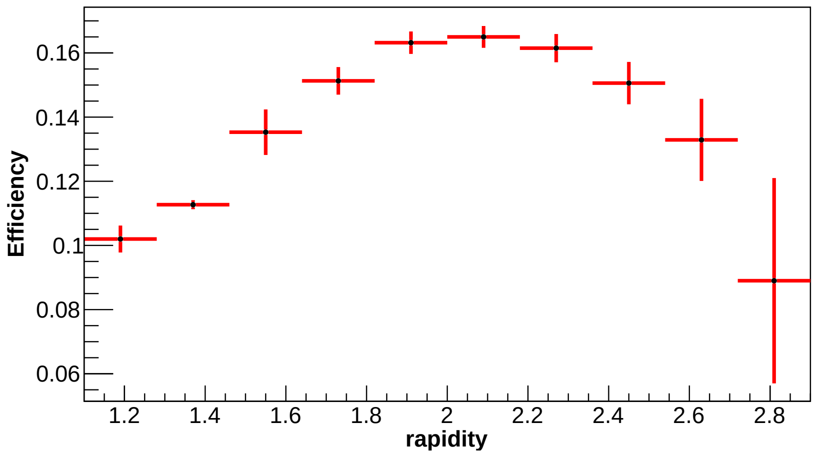


FIGURE 4.12: Efficiency plot of $J/\psi$

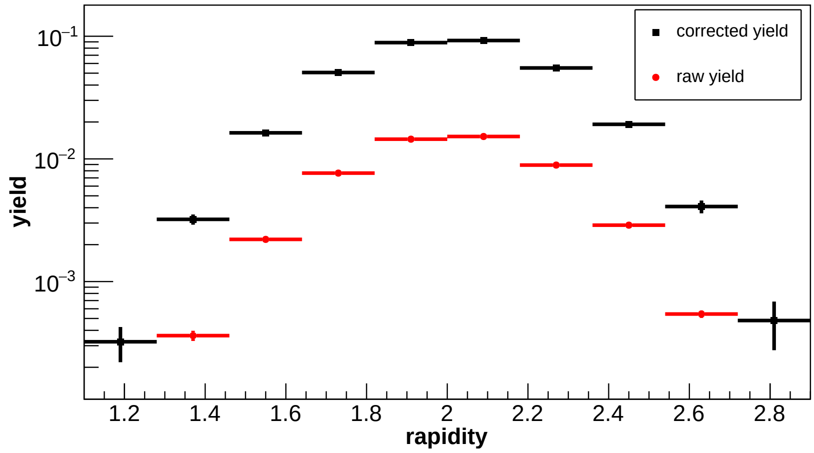


FIGURE 4.13: Raw and corrected yield of $J/\psi$

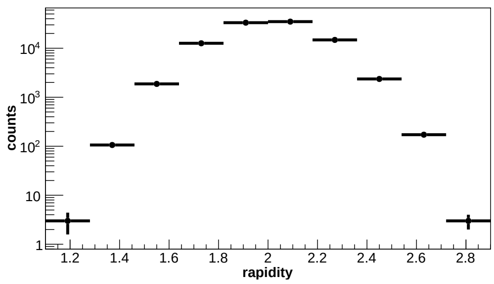


(a) Generated rapidity spectra

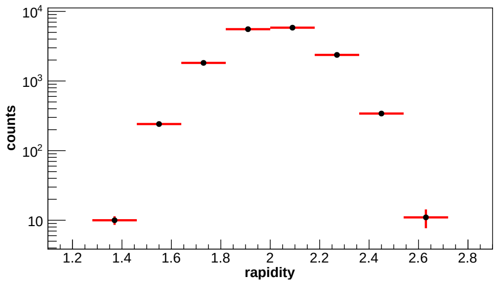


(b) Reconstructed rapidity spectra

FIGURE 4.14: Rapidity spectra for $\psi'$

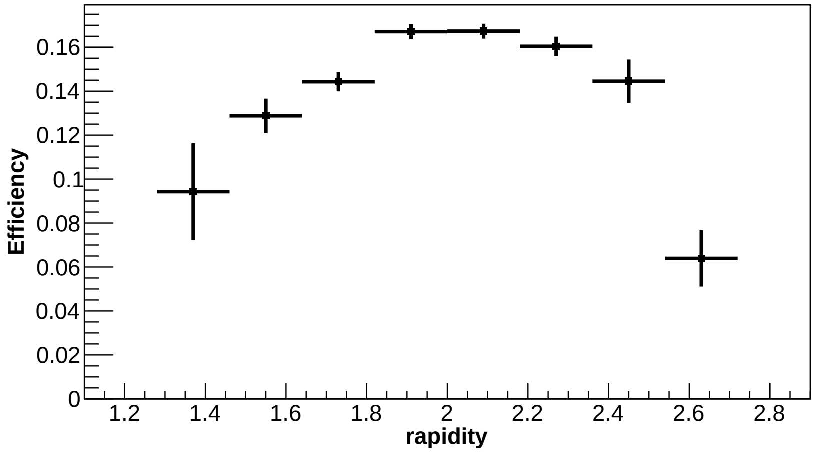


FIGURE 4.15: Efficiency plot of $\psi'$

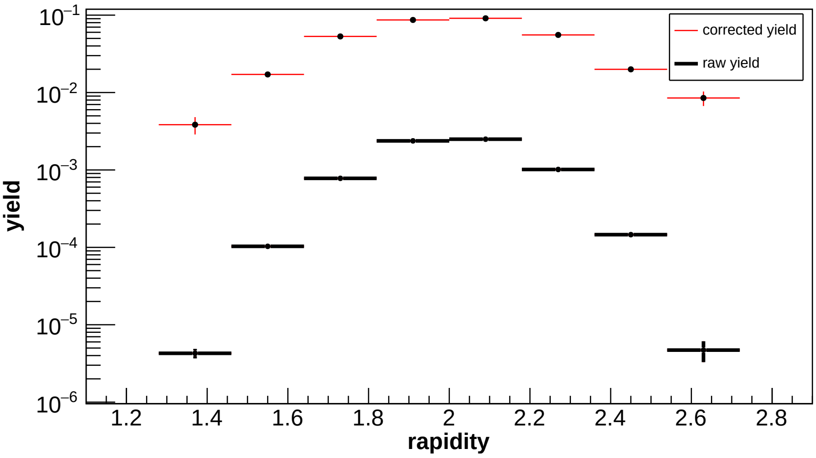


FIGURE 4.16: Raw and corrected yield of $\psi'$

From the plot of efficiecny in rapidity regime we can say that efficiency in mid rapidity is $\sim 16\%$.

# Chapter 5

# Result and Future outlook

## 5.1 Comparison of GEANT3 and GEANT4

In the chapter no.-4 of analysis, we tried comparing two different types of transport engine, i.e., GEANT3 and GEANT4 in CBM MuCh setup. From the study, we found the increment in the number of secondary particles with GEANT4 transport engine, whereas primary particles remain the same. Secondary particles increase by approximately 17% in 1st, 40% in the 2nd station, 85% in 3rd and approx 100% in 4th station. Observation from $p$ and $p_T$ spectra from each station also show the increase in the secondary particles.

## 5.2 Signal to background ratio of $J/\psi$

Signal to background ratio for $J/\psi$ found to be around $\sim 16.67$. The background is fitted with 4th order polynomial function and signal with Gaussian function taking $\mu = 3.1$ with fitting $\mu \pm 3\sigma$. The value obtained is with the cuts applied, as shown in table no-4.2.

## 5.3 Yield of $J/\psi$ and $\psi'$

We simulate the data from Pluto and UrQmd event generator in CBM chain to obtain efficiency and yield at 25 AGeV. The efficiency obtained for both the $J/\psi$ and $\psi'$ is around 15%. The value of yield is tabulated table no.-4.3 and 4.4 of chapter 4. As seen data from the table no- 4.3 and 4.4 the yield per event at lower momentum is higher for $J/\psi$ and at higher momentum $\psi'$ has higher yield per event.

In rapidity regime also it is found that the efficiency to be around 16% for both the particles in mid-rapidity region. It can be concluded from two different observation (Efficiency in both $p_T$ and rapidity regime ) that the detector has around 15% to 16% efficiency. The efficiency shows that the detector is not biased.

## 5.4 Future work

As the detector is in a developing stage, one can contribute it to build in a realistic manner by simulation of CBM chain. In the future, one can find the efficiency in $p_T$ and rapidity regime to check the $4\pi$ acceptance of the detector at SIS-300 energy. Here, we have done for $J/\psi$ and $\psi'$; one can work on different particles. And further simulation can be done with different transport engine and using different geometry setup.

# Bibliography


[1] P. P. Bhaduri, "Charmonium Production and Detection in High Energy Nuclear Collisions at FAIR"(2014).

[2] P.P. Bhaduri and S. Chattopadhya, Phys.Rev.C 81, 034906(2010)

[3] Lecture Notes in Physics 814 The CBM Physics Book.

[4] P.P.Bhaduri, P.Hegde, H.Satz and P.Tribedy, Lect. Notes Phys. **785**, 179 (2010) $doi : 10.1007/978 - 3 - 642 - 02286 - 9_5$ [arXiv:0812.3856 [hep-ph]].

[5] Ramona Vogt, Ultrarelativistic Heavy-Ion Collisions, Elsevier (2007).

[6] W. Heisenberg, Z. Phys. 101 (1936) 533; Z. Phys. 113 (1939) 61.

[7] R.Chatterjee, L.Bhattacharya and D.K.Srivastava, Lect. Notes Phys. **785**, 219 (2010) $doi : 10.1007/978 - 3 - 642 - 02286 - 9_7$ [arXiv:0901.3610 [nucl-th]].

[8] The CBM Collaboration, "Technical Design Report for the CBM"(2014).

[9] B.Friman, C.Hohne, J.Knoll, S.Leupold, J.Randrup, R.Rapp and P.Senger, Lect. Notes Phys. **814**, pp.1 (2011). $doi : 10.1007/978 - 3 - 642 - 13293 - 3$

[10] C. Patrignani *et al.* [Particle Data Group], Chin. Phys. C **40**, no. 10, 100001 (2016). $doi : 10.1088/1674 - 1137/40/10/100001$

[11] D. J. Gross and F. Wilczek, Phys. Rev. Lett. **30**, 1343 (1973). doi:10.1103/PhysRevLett.30.1343

[12] S. A. Bass *et al.*, Prog. Part. Nucl. Phys. **41**, 255 (1998) [Prog. Part. Nucl. Phys. **41**, 225 (1998)] $doi : 10.1016/S0146 - 6410(98)00058 - 1[nucl - th/9803035]$.

[13] C.-Y. Wong, hep-ph/0509088;

[14] The CBM Collaboration, "Technical Design Report for the CBM"(2014).

[15] D. Griffiths, Weinheim, Germany: Wiley-VCH (2008) 454 p

[16] www-hades.gsi.de/pluto.